Am J Physiol Cell Physiol 329: C2064–C2078, 2025.
First published November 19, 2025; doi:10.1152/ajpcell.00419.2025

american physiological society

AMERICAN JOURNAL OF PHYSIOLOGY
CELL PHYSIOLOGY

RESEARCH ARTICLE

Adaptation of the endplate in skeletal muscle of Homer 2$^{-/-}$ mice

Paola Lorenzon,[1] Stefano Amoretti,[2] Sandra Furlan,[3] Barbara Ravara,[2] Annalisa Bernareggi,[1] Marina Sciancalepore,[1] Roberta Sacchetto,[4] Aram Megighian,[2] Sandra Zampieri,[2,5] Alessandra Nori,[2]† and Pompeo Volpe[2]

[1]*Department of Life Sciences, University of Trieste, Trieste, Italy;* [2]*Department of Biomedical Sciences, University of Padova, Padova, Italy;* [3]*Institute of Neuroscience, National Research Council, Padova, Italy;* [4]*Department of Comparative Biomedicine and Food Science, University of Padova, Padova, Italy; and* [5]*Department of Surgery, Oncology and Gastroenterology, University of Padova, Padova, Italy*

Abstract

At the neuromuscular junction, nicotinic acetylcholine receptor (nAChR) dynamics are regulated in a nerve- and activity-dependent manner. Correlated local alterations in myoplasmic $[Ca^{2+}]_i$, induced by IP_3-sensitive subsynaptic Ca^{2+} stores, have been proposed to signal motor endplate adaptation to motor neuron stimulation. Accordingly, there is evidence for a modulatory role of Ca^{2+}/calmodulin-dependent protein kinase IIβ (CaMKIIβ) in the sorting, targeting, and/or incorporation of nAChRs into the postsynaptic membrane. As the scaffold protein Homer 2 emerges as a key player in integrating downstream postsynaptic signaling pathways, this study investigated the possible involvement of Homer 2 in the molecular mechanism controlling nAChR dynamics. Using Homer 2$^{-/-}$ transgenic mice, it was found that Homer 2 ablation leads to a chronic adaptation of the endplate characterized by: *1*) reduction in nAChR activity due to slower insertion of nAChRs into the endplate; *2*) reduced subsynaptic IP_3R1 content and IP_3-releasable Ca^{2+}; and *3*) impaired colocalization of CaMKIIβ with nAChRs. Overall, the present results demonstrate that Homer 2 ablation produces a significant alteration in endplate nAChR dynamics, which is associated with impaired organization of the subsynaptic IP_3-driven Ca^{2+} signaling mechanism.

NEW & NOTEWORTHY This research sheds light on the role of Homer 2 in organizing the subsynaptic microdomain, where nAChRs, IP_3R1s, and CaMKIIβ assemble to regulate nAChR dynamics. The present results point to a novel type of endplate instability, which may have implications for understanding neuromuscular junction function and related disorders.

endplate; Homer 2; neuromuscular junction; plasticity

INTRODUCTION

It is known that in both peripheral and central synapses, the density of the neurotransmitter receptors contributes to synaptic plasticity. In both types of synapses, receptors are highly dynamic and are constantly exchanged between the plasma membrane and intracellular compartments (1). At the neuromuscular junction (NMJ) of skeletal muscle, the sequential labeling of nicotinic acetylcholine receptors (nAChRs) combined with in vivo time-lapse imaging unveiled the existence of three receptor pools: preexisting, newly inserted, and rapidly recycling. The latter is incorporated into the endplate within a few hours (~8 h) (2, 3) and is comparable in magnitude with that of newly synthetized receptors (~25% over 4 days) (3).

The dynamics of nAChRs are controlled in an activity-dependent manner (2–4), thus suggesting a possible molecular/cellular strategy for the rapid adaptation of the endplate geometry and its transmission efficacy, depending on the motor neuron stimulation pattern. At the NMJ, intracellular Ca^{2+} is a candidate for transducing the synaptic activity into physiological tasks. It has been proposed that neurotransmitter-driven electrical activity could generate postsynaptic IP_3-associated local Ca^{2+} signals regulating NMJ development and stabilization. In particular, a functional interplay between nAChR activity and IP_3-driven Ca^{2+} release has been proposed to generate local subsynaptic Ca^{2+} signals (5, 6). The IP_3R1 isoform prevails at the endplate (6) and, interestingly, its subsynaptic localization appears to be mainly controlled by innervation through a mechanism that relies on the electrical activity of the muscle (7). Moreover, a correlation between the endplate and the subsynaptic IP_3R1-stained volume has been demonstrated in innervated fibers (7). The above observations suggest the existence of a motor neuron-controlled nAChR/IP_3Rs cross talk.

Among the sensors that mediate the effects of activity-dependent subsynaptic Ca^{2+} signaling on endplate plasticity, one of the best candidates is the serine/threonine Ca^{2+}/calmodulin-dependent kinase II (CaMKII) due to its ability to respond to different frequencies of Ca^{2+} signaling (8).

†Deceased 1 February 2025.
Correspondence: P. Lorenzon (plorenzon@units.it).
Submitted 23 May 2025 / Revised 9 June 2025 / Accepted 14 November 2025

Mammalian skeletal muscles express several isoforms of CaMKII: γ, δ, β isoforms, and a nonfunctional kinase variant of the α-isoform labeled α-anchoring kinase protein (αkap). In skeletal muscle, three CaMKII pools were initially proposed: cytosolic, sarcoplasmic reticulum-bound, and nuclear (9). According to its localization, it is now known that CaMKII is essential to enable a correct release of Ca^{2+} from the sarcoplasmic reticulum to ensure a high work intensity (10) and to allow gene regulation during remodeling in endurance exercise and growth after atrophy (11). Evidence for CaMKIIβ expression at the endplate and its tight clustering with nAChRs was first provided by Martinez-Pena y Valenzuela et al. (12), who also demonstrated that inhibition of CaMKII activity significantly prevented nAChR recycling; thus, a possible modulatory role of CaMKII in the sorting, targeting, and/or fusion of nAChR-containing endocytic vesicles with postsynaptic membranes has been suggested. In line with the hypothesis that CaMKII controls nAChR recycling at the endplate, it has recently been reported that deregulation of CaMKIIβ contributes to NMJ destabilization in specific pathological conditions (13).

The functional interaction between nAChR activity, IP_3-induced Ca^{2+} release (generating local Ca^{2+} signals), and CaMKIIβ expression beneath the endplate suggests the existence of a subsynaptic microdomain in which the different players—nAChR, IP_3R1, CaMKIIβ—interact with each other and regulate nAChR turnover. In this context, scaffolding proteins could also play a crucial role. Interestingly, the scaffolding protein Homer 2 has been shown to be localized in human and rodent NMJs and to be under the direct control of motor nerves, as inferred by its rapid and extensive downregulation following in vivo denervation of rat skeletal muscles (14, 15). Pulldown assays identified Homer 2 and NFATc1 as molecular partners, and Homer 2 has been shown to be part of the calcineurin-NFATc1 signaling pathway during NMJ adaptation to disuse and exercise (14, 15). However, Homer 2 may play additional yet unknown roles in the integration of other molecular players belonging to different synaptic signaling pathways (16). Interestingly, Homer proteins have already been proposed to interact with IP_3R1 in skeletal muscle (17) and nonskeletal muscle tissues (18).

Regarding the role of Homer 2 in the NMJ, we recently reported a reduction in endplate volume in single isolated fibers of the flexor digitorum brevis (FDB) from Homer 2$^{-/-}$ mice. This reduction formally resembles the effects of denervation in vivo. Unlike denervation, however, the reduction in endplate volume was less severe, and Homer 2 ablation did not result in any transition in nAChR isoform expression, that is, from ε-nAChRs (adult) to γ-nAChRs (embryonic), and distribution of nAChRs, which remained confined to the endplate region (19). Interestingly, altered cross-linking activity of the Homer protein was found to correlate with NMJ integrity in a mouse model of experimentally induced autoimmune myasthenia gravis. This observation confirms the role of Homer proteins in endplate adaptation (20).

Based on the availability of transgenic Homer 2$^{-/-}$ mice, the present work was carried out to further characterize the role of Homer 2 at the endplate level. We found that Homer 2 ablation caused endplate adaptation due to impaired nAChR dynamics with normal electromyography (EMG) profiles. This adaptation was associated with both altered organization of subsynaptic IP_3-sensitive compartments and CaMKIIβ distribution.

MATERIALS AND METHODS

Mice and Transgenic Mice

All the animals used in the present study were bred and housed in the certified animal facility at the University of Trieste. Mice had free access to food and water and were maintained in a 12-h light/12-h dark cycle. Transgenic Homer 2$^{-/-}$ mice (18) have been generously provided by Paul F. Worley (Johns Hopkins School of Medicine, Baltimore, MD). C57BL/6 mice were used to produce Homer 2 heterozygotes that were crossed to generate WT and Homer 2$^{-/-}$-mice to obtain animals with a more similar genotype. Fertility and body weight of WT and Homer 2$^{-/-}$ mice were checked, and no difference was detected between the two experimental groups. For blood sampling, mice were euthanized by inhalation of CO_2, and blood was collected after decapitation. For muscle dissection, mice were euthanized by cervical dislocation. For electromyography (EMG) recordings, mice were anesthetized using ketamine (0.15 mg/10 g body wt).

All the procedures carried out on mice were approved by the local Animal Care Committee and in agreement with the European legislation (2010/63/EU).

Isolation of Fibers from Flexor Digitorum Brevis Muscles

Isolated muscle fibers and bundles were obtained from flexor digitorum brevis (FDB) muscles of 6–8-wk-old Homer 2$^{-/-}$ and WT male mice.

Isolated muscle fibers were prepared from both hindlimb foot muscles of a single mouse for each preparation as described in detail elsewhere (21). In brief, immediately after the dissection, FDB muscles were enzymatically treated for 1 h in ice and 1 h at 37 °C with Type I collagenase 0.3% (wt/vol; C0130, Merck Life Science) in Tyrode's solution containing (in mM): NaCl 137, KCl 2.7, $MgCl_2$ 1, $CaCl_2$ 1.8, Na_2HPO_4 0.35, $NaHCO_3$ 12, HEPES 25.2, D-glucose 5.5, pH 7.4 NaOH supplemented with 100 U/mL penicillin, 100 µg/mL streptomycin, and 10% fetal bovine serum (Cat. No. F4135, Merck Life Science). Single fibers were isolated by mechanical dissociation with Pasteur pipettes with decreasing tip diameters and allowed to settle on Matrigel-coated (1 mg/mL; Cat. No. 354234, BD Biosciences) glass coverslips accommodated in 35-mm Petri dishes. Cultures were maintained in Tyrode's solution at 37°C in a humid air atmosphere containing 5% CO_2.

Recording of nAChRs Single-Channel Activity

Electrophysiological recordings were carried out on isolated FDB fibers from WT and Homer 2$^{-/-}$ mice in Tyrode's solution at room temperature. Single-channel recordings were performed using a MultiClamp 700B amplifier (Molecular Devices) after achieving a giga seal and when the baseline was stable. Signals were sampled at 50 kHz, filtered at 2 kHz with a low-pass Bessel filter, and analyzed by the pCLAMP 11.2 software package (Molecular Devices), using a threshold crossing criterion. All records were performed in the presence of 200 nM ACh (Cat. No. A6625, Merck Life Science), and for each stable patch, the time of recording (2–10 min)

was set to acquire at least 500 events. The open channel probability (NP_o) was calculated using the formula:

$$NP_o = (t_o/T),$$

where t_o is the total open time over the time T, and N is the number of channels in the patch. All analysis was performed at +60 mV pipette potential.

The exclusive presence of the ε-nAChRs isoform was confirmed by analyzing the unitary current amplitude and the open-time distribution. To examine the mean open time with accuracy, only traces with single-channel openings were considered for the analysis. Moreover, single-channel conductance was estimated from the slope of the regression line obtained by plotting the current amplitude against the pipette potentials (V_p) at +40, +60, and +80 mV (19).

Experiments were carried out on FDB muscle fibers obtained from 3 WT mice and 11 Homer 2$^{-/-}$ mice.

RNA Extraction and Quantitative RT-PCR

Frozen FDB tissue samples were ground to a fine powder under liquid nitrogen, and total RNA was extracted using the Trizol method, following the manufacturer's instructions and including a glycogen coprecipitating step. Reverse transcription was performed on 1 μg of total RNA using the SuperScript VILO cDNA Synthesis kit (Cat. No. 11754050, Thermo Fisher Scientific). Specific primers for *AChRa1* were designed with the Primer3 software (Whitehead Institute for Biomedical Research; http://frodo.wi.mit.edu/), and their thermodynamic specificity was determined using BLAST sequence alignments (US National Center for Biotechnology Information, NCBI) and Vector NTI Software (Thermo Fisher Scientific). Primers sequences for cyclophilin A (PPIA), TATA box-binding protein (TBP1), and hypoxanthine-guanine phosphoribosyltransferase (HPRT1) were already published by Gambara et al. (22). Quantitative RT-PCR was performed in triplicate in a CFX96 Thermal Cycler (Bio-Rad, Hercules) using SYBR Green chemistry. A melt-curve analysis was performed at the end of each experiment to verify that a single product per primer pair was amplified. PPIA, TBP, and HPRT1 were used as reference genes, and normalization was performed by the ΔCT method using PPIA; the same data trends were obtained with all reference genes.

Primers sequences were as follows: m_Chrna1_fw 5′-GGAGGACCACCGTGAGATTG-3′ and m_ Chrna1_rv 5′-GCCAGATCTTTTCCGAGGGG-3′.

Experiments were carried out on FDB muscles obtained from seven WT and eight Homer 2$^{-/-}$ mice.

nAChRs Turnover

To investigate the nAChR turnover, we used an nAChR labeling protocol based on two different α-bungarotoxin-conjugated species as previously described (3, 23). α-Bungarotoxin (4 μg/mL) conjugated to Alexa Fluor 647 (α-BuTX-647; Cat. No. B35450, Thermo Fisher Scientific) was injected in the FDB muscle in both hindlimbs in 6–8-wk-old Homer 2$^{-/-}$ and WT male mice to mark the preexisting nAChRs. After either 4 or 10 days, FDB muscles were excised, pinned onto a Sylgard-coated Petri dish, and then mechanically separated into individual bundles composed of 10–20 muscle fibers. FDB bundles were then fixed in 4% (vol/vol) paraformaldehyde in PBS for 30 min at room temperature and quenched in PBS containing 0.24% (wt/vol) NH_4Cl. The collected bundles were exposed for 2 h, at room temperature, to 4 μg/μL α-BuTX conjugated to Alexa Fluor 488 (α-BuTX-488; Cat. No. B13422, Thermo Fisher Scientific) to mark newly formed nAChRs.

In a subset of experiments, at 4 or 10 days, muscle bundles were permeabilized in PBS containing 0.5% (vol/vol) Triton X-100 for 2 h at room temperature and then incubated overnight at 4°C with α-BuTX-555 (2 μg/mL in PBS; Cat. No. B35451, Thermo Fisher Scientific). This labeling procedure was devised to detect the subsynaptic intracellular pool of nAChRs, as reported by Zelada et al. (24).

Bundles were mounted with Dako fluorescence mounting medium on glass slides. High-resolution images of individual NMJs were acquired using a Zeiss LSM 900 confocal microscope equipped with a Plan-Neofluar ×40/0.45 (NA) oil immersion objective. To reduce cross talk, the laser excitation line, power intensity, and emission range were chosen based on the specific fluorophore of each sample. Laser intensity was maintained constant throughout the acquisition of all samples.

Fluorescent intensity was quantified using ImageJ software (25). Fluorescence intensity was quantified on z-projected images encompassing the entire field of view, typically containing 10–15 NMJs per field. Background signal was removed by applying a consistent threshold, and the integrated density was measured for each fluorescence channel. A fluorescence intensity value was obtained for both α-BuTX-647 and α-BuTX-555, and the ratio of their intensities was subsequently calculated.

For each set of experiments, data were obtained on FDB bundles from three WT and three Homer 2$^{-/-}$ mice.

Immunofluorescence for Neural Cell Adhesion Molecule and Myosin Heavy Chain-Embryonic in FDB Muscles

Immunostaining for neural cell adhesion molecule (N-CAM) and myosin heavy chain-embryonic (MHC-emb) was carried out on 10-μm-thick serial cryosections from WT and Homer 2$^{-/-}$ FDB. Sections were fixed in methanol for 15 min at −20 °C and then incubated with blocking reagent M.O.M. (Mouse on Mouse; Cat. No. MKB-2213-1 Vector Laboratories) to block endogenous mouse immunoglobulins for 10 min at room temperature. Sections were then incubated with 10% goat serum in PBS (Cat. No. G9023, Merck Life Science) for 20 min at room temperature and incubated with either rabbit polyclonal antibody directed against N-CAM (Cat. No. AB5032; Chemicon, Millipore) diluted 1:200 in PBS supplemented with 2% goat serum, or mouse monoclonal antibody directed against MHC-emb (NCL-MHCd, Novocastra) 1:20 diluted in TBS, overnight at 4 °C. Sections were then rinsed three times for 5 min in PBS, blocked with 10% goat serum in PBS for 10 min and then incubated for 1 h at room temperature with goat anti-rabbit Alexa Fluor 594 (Cat. No. A11012, Thermo Fischer Scientific) 1:500 diluted in PBS or with goat anti-mouse Alexa Fluor 488 and Alexa Fluor 594-wheat germ agglutinin (WGA) (Cat. Nos. A11001 and W11262, Thermo Fischer Scientific) 1:500 diluted in PBS. After washing, sections were coverslipped using ProLong Diamond Antifade Mountant with DAPI dye (Cat. No. P36962, Thermo Fischer Scientific) and observed under a Zeiss microscope connected to a Leica DC300F camera. N-CAM-positive fibers were counted on captured images, using

Fiji ImageJ software (v. 2.1.0/1.53c, National Institutes of Health) and expressed as the number of positive fibers per total number of fibers detected in the biopsy area (~200 muscle fibers).

FDB muscles were obtained from six WT and six Homer 2$^{-/-}$ mice.

C-Terminal Agrin Fragment Assessment

Circulating levels of C-terminal agrin fragment (CAF) were determined in the plasma of WT and KO mice, using a commercially available enzyme-linked immunosorbent assay (ELISA) kit (Rat Agrin ELISA kit, Cat. No. Ab267586, Abcam) following the manufacturer's instructions. All samples were assessed in duplicate and were diluted four times using the appropriate diluent purchased with the kit. CAF concentrations were read in a microplate ELISA reader (Tecan, Infinite M200, Thermo Fisher Scientific). To assess plasma CAF concentrations, a standard curve (loaded with known and increasing CAF concentrations) was prepared and read at 450 nm. CAF concentrations were interpolated from the standard curve and then corrected for the initial sample dilution to obtain accurate measurements.

CAF assessment was performed on samples obtained from four WT and seven Homer 2$^{-/-}$ mice.

nAChR, IP$_3$R1, and CaMKIIβ Stainings in Single FDB Muscle Fibers

In single FDB muscle fibers, the double labeling of nAChRs/IP$_3$R1s and nAChRs/CaMKIIβ was carried out 24 h after dissociation. Fixation of fibers was done on coverslips with a solution of 4% (vol/vol) paraformaldehyde in PBS for 15 min at 4 °C. Fibers were then permeabilized in PBS + Triton X-100 0.3% (vol/vol) for 15 min and incubated in a blocking solution containing 2% M.O.M. Blocking Reagent (Cat. No. MKB-2213-1, Vector Laboratories) in PBS for 30 min. After permeabilization, fibers were stained for IP$_3$R1s with antibodies developed by Volpe et al. (26) or for CaMKIIβ with the monoclonal antibody 13-9800 (Thermo Fisher Scientific). Both primary antibodies were diluted 1:100 in blocking solution and incubated overnight at 4 °C. After washing, muscle fibers were incubated for 1 h at room temperature with the secondary goat anti-mouse Alexa Fluor 594-conjugated antibody (1:300 in PBS; Cat. No. A-11005; Thermo Fisher Scientific). After IP$_3$R1s or CaMKIIβ staining, nAChRs were labeled by 2.5 μg/mL Alexa Fluor 488-α-BuTX (α-BuTX-488; Cat. No. B13422, Thermo Fisher Scientific) in PBS for 1 h at room temperature. After staining, fibers were washed three times with PBS and finally rinsed with distilled water and mounted with ProLong Gold Antifade Mountant with DAPI (Cat. No. P36931, Thermo Fisher Scientific) on a microscope glass.

Stainings were performed in at least four independent FDB fiber cultures for each experimental group.

Volumetric Analysis of nAChR and IP$_3$R1 Staining

Distribution of nAChRs and IP$_3$R1s was analyzed on images acquired by a Nikon C1 confocal microscope (Melville, NY) using a Plan-Apochromat ×60/1.4 (NA) oil immersion objective. Optical images were collected at either 0.30 or 0.35 μm *z*-resolution by sequential line scanning. Volumetric analysis of the endplate nAChRs and corresponding subsynaptic IP$_3$R1s staining was carried out by applying Fiji ImageJ software (v. 2.1.0/1.53c, National Institutes of Health) as described in detail in Volpe et al. (7).

Analysis was carried out in FDB fibers of independent cell cultures obtained from four WT and four Homer 2$^{-/-}$ mice.

Colocalization Analysis of nAChR and CaMKIIβ Staining

Double-stained images for nAChRs and CaMKIIβ were acquired by the super resolution microscope Zeiss Elyra7 (Oberkochen, Germany) using a Plan-Apochromat ×63/1.4 (NA) oil immersion objective. Optical images were collected by sequential line scanning at 0.25 μm *z*-resolution. Quantitative colocalization analysis of nAChRs and CaMKIIβ was performed using the Coloc function of Fiji ImageJ software (v. 2.1.0/1.53c, National Institutes of Health) on images obtained by structured illumination (lattice SIM) for all channels. The region of interest (ROI) for the colocalization measurements corresponded to the endplate volume. This ROI was set using the same method as for the volumetric analysis of nAChR and IP$_3$R1 stainings, described in detail in Volpe et al. (7). The colocalization of nAChRs and CaMKIIβ was calculated after the background subtraction from each captured image of the *z*-stack covering the endplate volume. In each fiber and for each of the two channels, the background value was set at the maximum fluorescent value recorded outside the ROI. Three-dimensional reconstruction of endplates and corresponding synaptic CaMKIIβ distribution was carried out with IMARIS software (trial version) on structured illumination images upon application of the image reconstruction algorithm by Zeiss.

Colocalization analysis was performed in FDB fibers of independent cell cultures obtained from three WT and three Homer 2$^{-/-}$ mice.

Ca^{2+} Measurements

FDB muscle fibers were plated on 18-mm coverslips and incubated with 1 μM Fluo-4/AM (Cat. No. F14217, Thermo Fisher Scientific), 0.02% pluronic F-127 (Cat. No. P2443, Merck Life Science), 200 μM sulfinpyrazone (Cat. No. S9509, Merck Life Science), and 2 μg/mL Alexa Fluor555 conjugate (α-BuTX-555; Cat. No. B35451, Thermo Fisher Scientific) for 30 min at 37 °C in mKRB medium (in mM: 140 NaCl, 2.8 KCl, 2 $MgCl_2$, 10 HEPES, and 1 $CaCl_2$, pH 7.4) supplemented with 10 mM glucose. After washing, coverslips were mounted in Ca^{2+}-free, EGTA-containing (100 μM) mKRB and visualized on an inverted microscope (DMi8 Thunder Imager 3-D Cell Culture; Leica Microsystems) by a ×20 ultraviolet-permeable objective (HC PL FLUOTAR 340; Leica Microsystems). Fluo-4 was excited with the white line of a CoolLED pE-340fura (CoolLED Limited). Fluorescent signal was collected with a Leica DMi8 GFP-filter set. Fluo-4 images were acquired every 50 ms, with a 40-ms exposure time by a Hamamatsu Flash 4.0 V3 camera (Hamamatsu Photonics). Cyclopiazonic acid (20 μM) (CPA; Cat. No. C1530, Merck Life Science) was added to release Ca^{2+} from the sarcoplasmic reticulum. At the end of each experiment, α-BuTX-555 was excited by the 555 nm line of LED8 (Leica Microsystems) to visualize the NMJ and to select the corresponding ROIs. Images were background-subtracted and analyzed with LAS X Premium

(Leica Microsystems), calculating the ratio F/F_0 between the Fluo-4 fluorescence emission collected at each frame (F) and that collected at the beginning of the experiment (F_0) in the ROIs.

Ca^{2+} measurements were carried out in FDB fibers of independent cell cultures obtained from four WT and four Homer 2$^{-/-}$ mice.

Electromyography

Electromyographic (EMG) recordings were performed on the FDB muscles of WT and Homer 2$^{-/-}$ mice at room temperature (20°C–22°C). Stainless steel monopolar electrodes (28-gauge; Grass-AstroMed) were used as both stimulating and recording electrodes. In anesthetized mice, EMG recordings were performed by inserting a recording electrode into the center of the hindfoot, whereas the reference electrode was inserted between the second and third toes. Stimulating electrodes were fixed on a mechanical micromanipulator and lowered onto the sciatic nerve at the sciatic notch, exposed by cutting the overlying skin and partially separating the gluteus superficialis and biceps femoris muscles. The ground electrode was placed around the tail. Square wave pulses of fixed duration (0.5 ms), delivered by a stimulator (S88; Grass-AstroMed) through a stimulus isolator unit (SIU-5; Grass-AstroMed), were used to stimulate the nerve. The intensity of the stimulus was adjusted to obtain supramaximal nerve stimulation. Before stimulating the nerve, the presence of spontaneous electromyographic activity was checked for a period of 10 s. Nerve-evoked FDB compound muscle action potentials (CMAPs) were then recorded, stimulating the nerve first at 0.5 Hz for 20 s, then at 10 Hz and, after 10 s of recovery, at 30 Hz. Recorded signals were amplified with an extracellular amplifier (EXT-2B, NPI), digitized with an A/D interface (Cat. No. NI PCI-6221, National Instruments), and then fed to a PC for both online visualization and offline analysis using appropriate software (WinEDR, Strathclyde University; pCLAMP, Axon). Stored data were analyzed offline using the pCLAMP 11.2 software package (Molecular Devices), and the amplitude of all recorded CMAPs was measured. Tetanic stimulations (10 or 30 Hz) were analyzed, considering the amplitude of the first CMAP of each repetitive response as equal to 1.

Motor Performance Assessment

A wire hanging test was carried out to monitor the muscle endurance of WT and Homer 2$^{-/-}$ mice. In brief, the mouse was placed on a wire cage lid that was gently waved, forcing the animal to grip the wire. The lid was then turned upside down ~50 cm above the surface of a soft bedding material. The latency to fall was recorded (cutoff time: 120 s) in nine WT and nine Homer 2$^{-/-}$ mice.

Motor coordination and balance were assessed with an accelerating rotarod apparatus. Mice were placed on a rotating drum (3 cm diameter), and the latency to fall was recorded. The rotation speed increased linearly from 4 to 40 rpm over a 5-min trial in the habituation phase. Mice underwent a habituation phase, which consisted of three trials per day for 3 consecutive days. After the habituation phase, testing sessions were conducted at a constant speed of 40 rpm with a cutoff time of 300 s.

Statistical Analysis

Normality of data was assessed using both the Shapiro–Wilk and Kolmogorov–Smirnov normality tests to ensure robust evaluation of data distribution and to guide the choice of the proper statistical test. For parametric data, statistical significance was determined using an unpaired *t* test; for data that do not belong to a normal distribution, statistical analysis was performed using Mann–Whitney test. Relationships between volumetric analysis of the endplate and corresponding subsynaptic IP_3R1-stained volume were analyzed by Spearman's correlation test (for nonparametric data). Statistical significance between EMG data was analyzed using the Mann–Whitney test and applying a linear mixed model (LMM). Statistical significance was accepted at $P \leq 0.05$. Statistical analysis was performed using GraphPad Prism (v. 8.00; GraphPad Software), which was also used to create the graphs.

RESULTS

Reduced Synaptic nAChR Activity and Upregulation of AChRα1 Gene Expression in FDB Muscle Fibers of Homer 2$^{-/-}$ Mice

Endplate nAChR activity was assessed by the patch clamp technique in the cell-attached configuration on isolated FDB muscle fibers from both Homer 2$^{-/-}$ and WT mice; the mean open channel probability (NP_o) was measured. In both experimental groups, endplates were identified as a distinct roughness of the fiber surface using phase contrast microscopy (21). Channel openings were elicited using a pipette filling solution containing 200 nM ACh (Fig. 1*A*). As previously reported (19), the analysis of the nAChR single-channel activity from the recorded endplates confirmed the exclusive presence of the adult ε-nAChR isoform in both Homer 2$^{-/-}$ and WT FDB muscle fibers (19). As shown in Fig. 1*B*, NP_o was decreased by ~50% in Homer 2$^{-/-}$ FDB fibers as compared with the WT counterpart; this suggested a lower number of nAChR openings at the endplate.

Except for the most abundant nAChR subunit α1 (nAChR-α1), we were unfortunately unable to quantify the expression of the other subunits, as their corresponding mRNAs were below the detection limit. Intriguingly, quantitative RT-PCR analysis in Homer 2$^{-/-}$ mice reveals that the nAChR-α1 gene was upregulated by approximately sixfold compared with the WT counterpart (Fig. 1*C*). Such an upregulation could be a compensatory mechanism of the Homer 2$^{-/-}$ FDB muscle fibers to counteract the reduced number of functional nAChRs at the endplate level.

Biomarkers of Denervation/Regeneration, N-CAM and MHC-emb, Are Negative in FDB Fibers of Homer 2$^{-/-}$ Mice

The presence of the adult ε-nAChR isoform (19) and the absence of extrajunctional nAChRs seemed to exclude the occurrence of denervation of Homer 2$^{-/-}$ FDB fibers. To rule out denervation, apoptosis, and consequent regeneration, the expression of N-CAM and MHC-emb in FDB muscles was also monitored. In innervated and fully differentiated muscle fibers, N-CAM accumulates in the proximity of the NMJ,

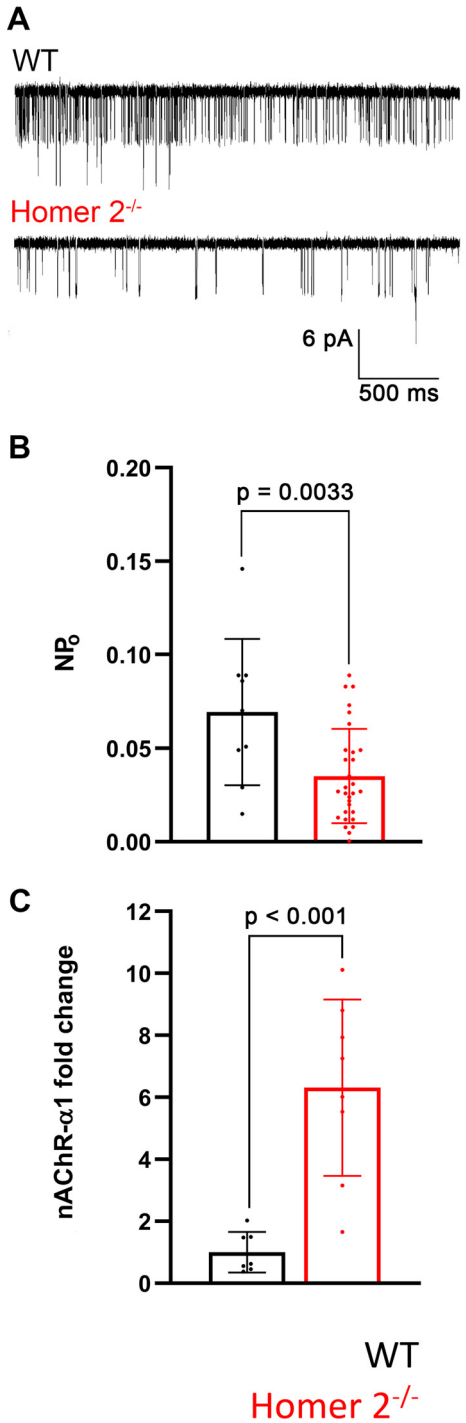

Figure 1. Endplate nAChRs activity and expression of AChR-α1 gene in FDB fibers of WT and Homer 2$^{-/-}$ mice. *A*: representative traces of single nAChR channel recordings from WT and Homer 2$^{-/-}$ endplates of isolated FDB fibers ([Ach] = 200 nM; V_p = +60 mV). *B*: mean open channel probability (NP_o) calculated from the recordings carried out in WT and Homer 2$^{-/-}$ FDB fibers (WT: 0.069 ± 0.039, n = 9 fibers from 3 mice; Homer 2$^{-/-}$: 0.035 ± 0.025, n = 30 fibers from 11 mice). *C*: qPCR analysis of nAChR-α1 mRNA in FDB muscles from WT (7 animals) and Homer 2$^{-/-}$ mice (8 animals). Values are expressed as the fold change over WT after normalization with the PPIA gene. Statistical differences were determined by an unpaired *t* test. Values are shown as means ± SD. FDB, flexor digitorum brevis; nAChR, nicotinic acetylcholine receptor; PPIA, primer sequences for cyclophilin A; WT, wild type.

whereas after denervation, the protein is reexpressed along the entire sarcolemma and in the sarcoplasm (27). In Homer 2$^{-/-}$ as well as in WT sections, no significant differences were observed with regard to the percentage of myofibers displaying sarcolemmal and/or diffuse sarcoplasmic N-CAM staining (Fig. 2, *A* and *B*). In addition, the absence of MHC-emb expressing myofibers in Homer 2$^{-/-}$ FDB cryosections confirmed the absence of regenerating fibers (Fig. 2*C*).

Taken as a whole, the above observations clearly indicate that muscle denervation and regeneration were not taking place in Homer 2$^{-/-}$ FDB muscles.

Circulating CAF Levels Were Similar in WT and Homer 2$^{-/-}$ Mice

Even if N-CAM and MHC-emb stainings excluded the occurrence of denervation/regeneration processes in Homer 2$^{-/-}$ FBD muscles, the reduced synaptic nAChRs activity in null Homer 2 FDB fibers suggests NMJ instability. It is well known that the integrity of the NMJ depends on both motor innervation and adequate levels of agrin, the motoneuron-derived proteoglycan. However, excessive cleavage of the neural agrin induced by neurotrypsin, produced by the motor neuron itself, is sufficient to cause severe NMJ destabilization in innervated fibers (28). NMJ destabilization is associated with higher plasmatic levels of the soluble C-terminal agrin fragment (CAF) and has been documented in conditions of "functional" denervation, that is, aging (29) and disuse (30). Based on this knowledge, experiments were carried out to assess whether a "functional" denervation could cause the reduced synaptic nAChR activity detected at Homer 2$^{-/-}$ endplates. Analysis of blood samples from WT and Homer 2$^{-/-}$ mice did not reveal, however, differences in CAF concentration between the two experimental groups (Fig. 3).

This result ruled out an altered cleavage of the stabilizing agent agrin as the main reason contributing to the reduced nAChR NP_o in endplates of Homer 2$^{-/-}$ FBD fibers.

Impaired nAChRs Turnover in FDB Fibers of Homer 2$^{-/-}$ Mice

To further explore the cellular processes leading to the reduced activity of the nAChRs, the turnover dynamics of the receptors at the NMJ of Homer 2$^{-/-}$ mice were investigated by a kind of pulse-chase nAChR labeling protocol, previously described by Röder et al. (23). In brief, after injection of α-BuTX-647 into FDB muscles of either Homer 2$^{-/-}$ or WT mice, muscles were harvested at postinjection *days 4* and *10*. At each time point, additional staining was performed with α-BuTX-488 to label newly inserted nAChRs, thus allowing quantification of fluorescent signals emitted by newly incorporated (α-BuTX-488 green fluorescent signal) and preexisting (α-BuTX-647 red fluorescent signal) receptors. At *day 4*, a reduced α-BuTX-488/α-BuTX-647 fluorescent signal ratio in Homer 2$^{-/-}$ NMJs was observed in comparison with WT ones, as judged by confocal image analysis: these results indicate an impaired incorporation of newly synthesized receptors (Fig. 4, *A* and *B*). At *day 10*, the ratio value became similar in NMJs from Homer 2$^{-/-}$ and WT mice, that is, the nAChRs turnover was delayed in NMJs of Homer 2$^{-/-}$ mice.

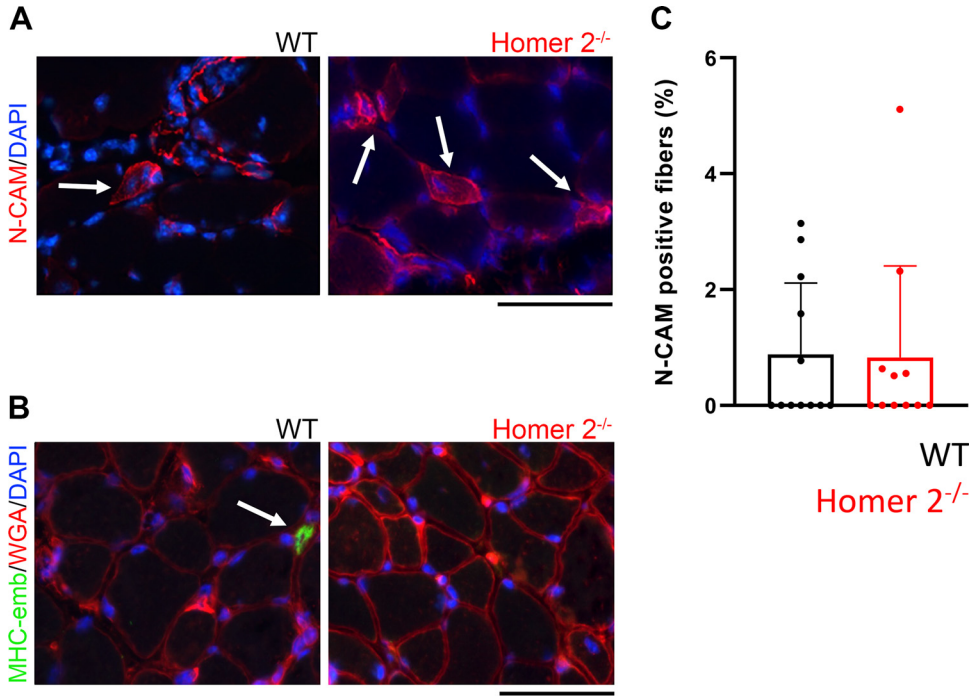

Figure 2. Biomarkers of denervation/regeneration in FDB muscles of WT and Homer 2$^{-/-}$ mice. *A*: representative images of N-CAM expression in FDB muscles from WT and Homer 2$^{-/-}$ mice. Arrows point to N-CAM-positive fibers. In both cases, N-CAM-specific staining was also visible in small blood vessels. Scale bar, 50 μm. *B*: quantification of N-CAM-positive fibers in WT and Homer 2$^{-/-}$ FDB muscles (WT: 0.88 ± 1.23%, from 6 mice; Homer 2$^{-/-}$: 0.83 ± 1.58%, from 6 mice). *C*: very few regenerating MHC-emb expressing fibers were detected in WT FDB muscles (0.25 ± 0.20%, from 6 mice), whereas Homer 2$^{-/-}$ muscles were negative. In *B* and *C*, values are shown as means ± SD, and statistical differences were determined by an unpaired *t* test. FDB, flexor digitorum brevis; MHC-emb, myosin heavy chain-embryonic; N-CAM, neural cell adhesion molecule; WT, wild type.

We also carried out experiments to quantify the intracellular nAChR pool at the NMJs. For this purpose, muscle bundles were permeabilized before labeling with α-BuTX-555. No differences in the intracellular nAChR pool were observed between NMJs from Homer 2$^{-/-}$ and WT mice, neither at *day 4* nor at *day 10*. These results rule out the possibility that the delayed nAChR turnover observed at Homer 2$^{-/-}$ mice NMJs was due to an impaired availability of the intracellular nAChR pool (Fig. 4, *C* and *D*).

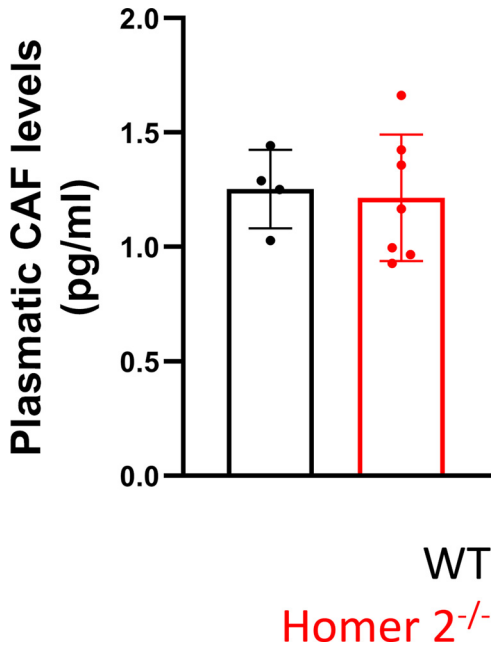

Figure 3. Plasmatic CAF levels in WT and Homer 2$^{-/-}$ mice. Quantification of the circulating levels of CAF in plasma samples from WT and Homer 2$^{-/-}$ mice. The mean CAF plasma concentration was similar in WT and Homer 2$^{-/-}$ mice: 1.25 ± 0.17 pg/mL (4 mice) and 1.21 ± 0.27 pg/mL (7 mice), respectively. Values are shown as means ± SD. CAF, C-terminal agrin fragment; WT, wild type.

Reduction of Subsynaptic IP$_3$R1-Stained Volume and Subsynaptic Releasable Ca^{2+} Content in FDB Fibers of Homer 2$^{-/-}$ Mice

A reduction in the endplate volume in single FDB fibers from Homer 2$^{-/-}$ mice has been recently reported (19). In the present work, we investigated whether the subsynaptic volume referable to IP$_3$R1 was altered in Homer 2$^{-/-}$ mice. The endplates were visualized using α-BuTX staining, and FDB fibers were immunolabeled with antibodies specific for IP$_3$R1, as described in detail in *Immunofluorescence for Neural Cell Adhesion Molecule and Myosin Heavy Chain-Embryonic in FDB Muscles*. Confocal scanning microscopy revealed a decrease of nAChR-staining associated with a decrease of IP$_3$R1-stained volume in fibers of Homer 2$^{-/-}$ mice; both reductions were similar, that is, ∼30%, as compared with the two mean volumes calculated in WT fibers (Fig. 5, *A* and *B*). It was also observed that the IP$_3$R1-stained volume corresponded to ∼40% of the endplate region in both WT and Homer 2$^{-/-}$ fibers, confirming a correlation between subsynaptic IP$_3$R1-stained volume and the endplate size in Homer 2 null FDB muscles as well (Fig. 6).

Synaptic IP$_3$-dependent local Ca^{2+} signals are required for NMJ stabilization (5, 6). Based on this knowledge, we carried out Ca^{2+} videoimaging experiments to quantify the subsynaptic Ca^{2+} releasable content in single fibers obtained from Homer 2$^{-/-}$ and WT mice. To this effect, 20 μM cyclopiazonic acid was applied to Fluo-4-loaded Homer 2$^{-/-}$ and WT fibers in Ca^{2+}-free solution to measure the total subsynaptic releasable Ca^{2+} content (Fig. 7*A*). The mean area values subtended by the intracellular calcium ([Ca^{2+}]$_i$) transients elicited by CPA were significantly different between the two groups. Specifically, the subsynaptic releasable Ca^{2+} pool

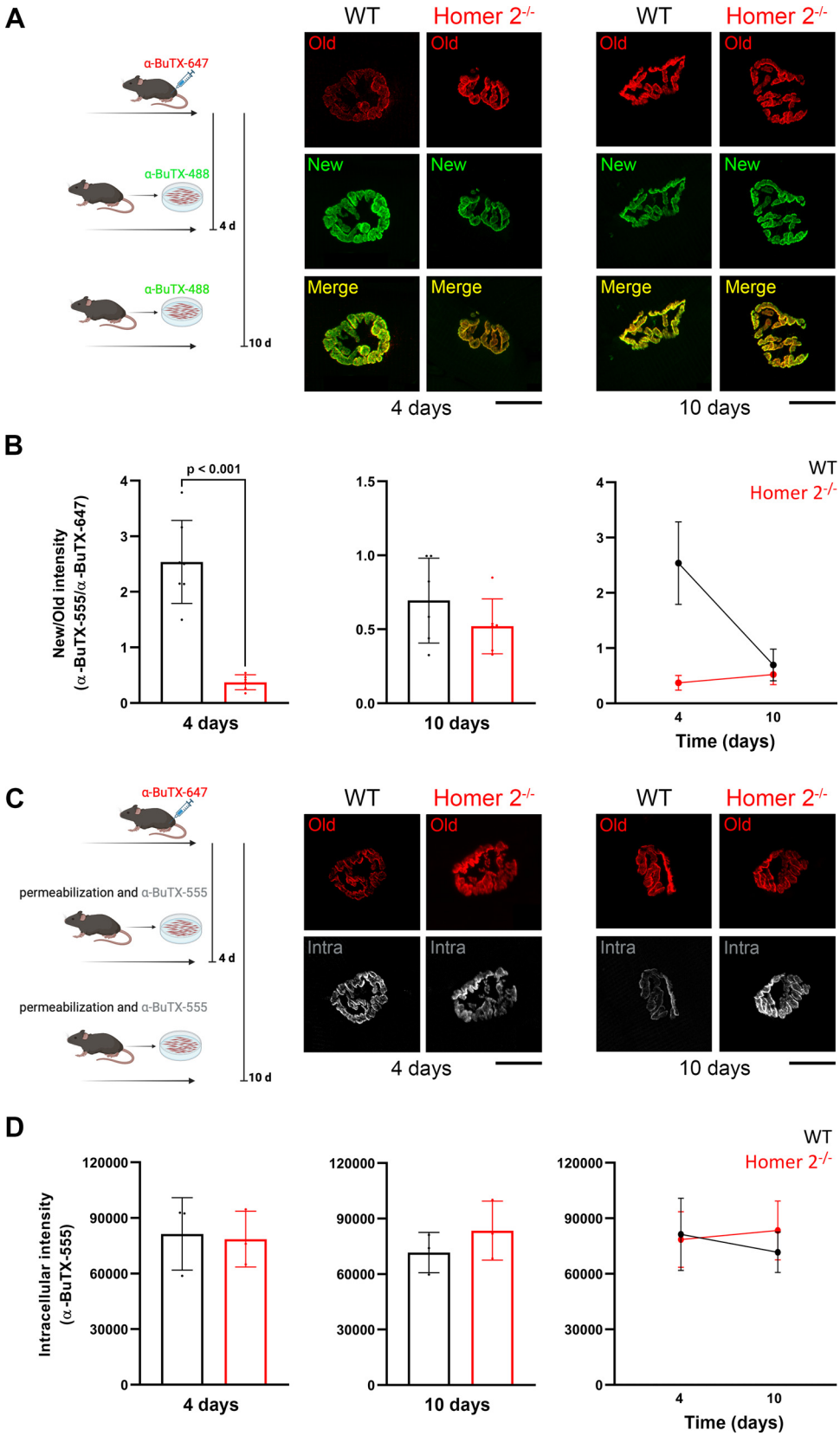

Figure 4. Slower nAChRs turnover in FDB fibers of Homer 2$^{-/-}$ mice. *A*, *left*: timeline of the pulse-chase nAChR labeling protocol (figure, in part, created with a licensed version of BioRender.com). *Right*: representative maximum intensity *z*-projections of fluorescent signals corresponding to α-BuTX-647 ("old" nAChRs) and α-BuTX-555 ("new" nAChRs), and overlay of both on *days 4* and *10* after labeling with α-BuTX-647. Scale bar, 20 μm. *B*: quantification of the α-BuTX-555/α-BuTX-647 fluorescent signal ratios calculated at 4 and 10 days in Homer 2$^{-/-}$ and WT NMJ. Each data point represents the mean ratio value from 10 to 15 endplates belonging to the same optical field (WT at 4 days: 2.54 ± 0.75, $n = 7$ optical fields; WT at 10 days: 0.69 ± 0.29, $n = 6$ optical fields; Homer 2$^{-/-}$ at 4 days: 0.37 ± 0.13, $n = 6$ optical fields; Homer 2$^{-/-}$ at 10 days: 0.52 ± 0.18, $n = 6$ optical fields). In the last graph, the mean fluorescent signal ratios are plotted vs. the experimental timepoints. *C*, *left*: timeline of the labeling protocol for the nAChR intracellular pool (figure, in part, created with a licensed version of BioRender.com). *Right*: representative maximum intensity *z*-projections of α-BuTX-647 fluorescent signals and corresponding intracellular nAChRs (pseudocolored gray) labeled by bundles permeabilization before the incubation with α-BuTX-555 on *days 4* and *10*. Scale bar, 20 μm. *D*: quantification of the intracellular α-BuTX-555 fluorescent signal calculated at 4 and 10 days in Homer 2$^{-/-}$ and WT NMJ. Each data point represents the mean ratio value from 10 to 15 endplates belonging to the same optical field (WT at 4 days: 81,377 ± 19,570, $n = 3$, optical fields; WT at 10 days: 71,649 ± 10,866, $n = 3$, optical fields; Homer 2$^{-/-}$ at 4 days: 78,569 ± 15,031, $n = 3$, optical fields; Homer 2$^{-/-}$ at 10 days: 83,496 ± 15,907, $n = 3$, optical fields). Statistical differences were determined by the Mann–Whitney *U* test. Values are shown as means ± SD. FDB, flexor digitorum brevis; nAChRs, nicotinic acetylcholine receptors; NMJ, neuromuscular junction; WT, wild type.

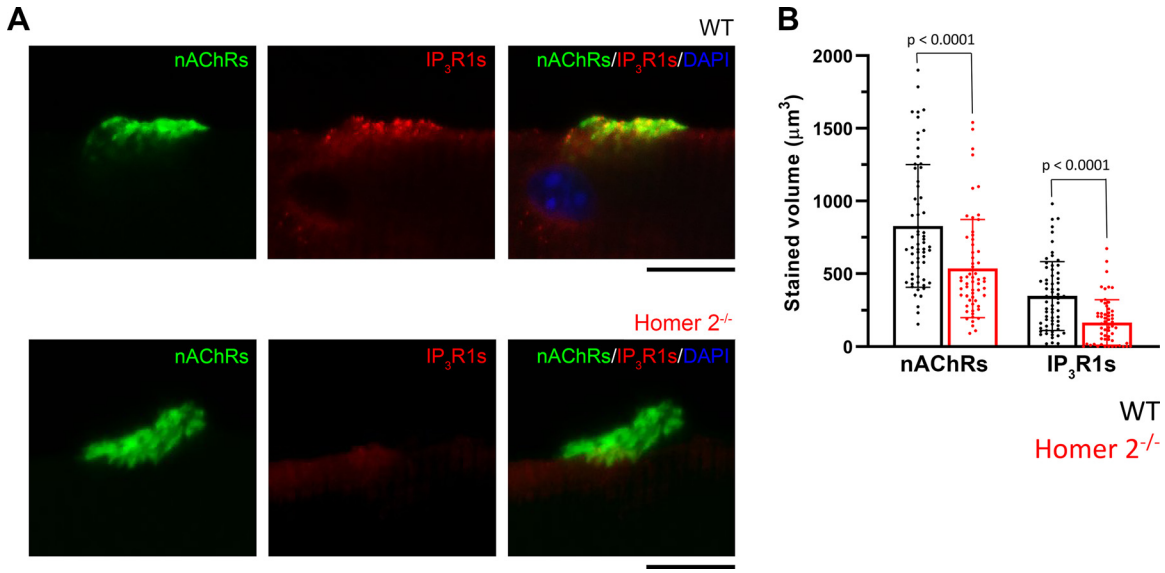

Figure 5. nAChR- and IP_3R1-stained volumes in FDB fibers of WT and Homer $2^{-/-}$ mice. *A*: representative nAChR- and IP_3R1-staining for WT and Homer $2^{-/-}$ FDB fibers. WT and Homer $2^{-/-}$ images are shown as maximum intensity projections of the green and red voxels detected in the plans covering the entire depth of the endplate (i.e., containing an α-BuTX visible signal). The total number of projected plans was 45 for WT and 22 for Homer $2^{-/-}$ images, respectively. Scale bar, 10 µm. *B*: nAChR- and corresponding IP_3R1-stained volumes from each observed fiber were shown as a scatter plot. In WT FDB fibers, the mean nAChR- and IP_3R1-stained volumes were 828.10 ± 422.90 µm^3 and 346.70 ± 236.20 µm^3 (n = 64 fibers, 4 animals). In Homer $2^{-/-}$ FDB fibers, the mean nAChR- and IP_3R1-stained volumes were 536.20 ± 337.10 µm^3 and 165.80 ± 156.20 µm^3 (n = 59 fibers, 4 animals). Values are shown as means ± SD, and statistical differences were determined by the Mann–Whitney *U* test. FDB, flexor digitorum brevis; nAChR, nicotinic acetylcholine receptor; WT, wild type.

was decreased by ~30% in Homer $2^{-/-}$ muscle fibers compared with WT fibers. The previously mentioned decrease in intracellular Ca^{2+} storage was not observed in extrasynaptic regions (Fig. 7*B*). This suggests that ablation of Homer 2 caused a specific effect on the subsynaptic intracellular Ca^{2+} stores, rather than a general alteration of cellular Ca^{2+} handling.

Colocalization of CAMKIIβ with nAChRs Was Reduced in FDB Fibers of Homer $2^{-/-}$ Mice

CaMKIIβ expression at the endplate level and its tight clustering with nAChRs have been previously reported by Martinez-Pena y Valenzuela et al. (31). Based on this knowledge, we designed experiments to investigate whether the absence of Homer 2 could induce an altered distribution of CaMKIIβ at the endplate. This question was crucial for understanding the role of Homer 2 in shaping the molecular architecture of the NMJ.

As for quantification of nAChRs/IP_3R1s by confocal microscopy, the endplate was stained with α-BuTX and immunolabeled with antibodies specific for CaMKIIβ in FDB single muscle fibers. Moreover, super-resolution fluorescence microscopy was used to achieve a better spatial resolution and accurately evaluate the kinase colocalization with

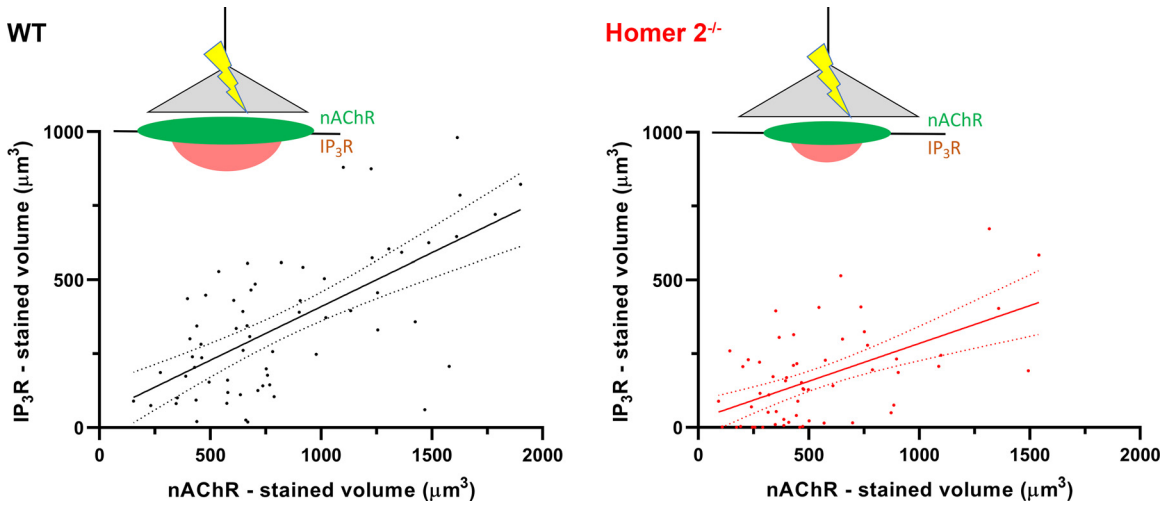

Figure 6. Endplate/IP_3R1-stained volume correlation in FDB fibers of WT and Homer $2^{-/-}$ mice. Correlation plots of nAChR- vs. corresponding IP_3R1-stained volumes were calculated from data shown in Fig. 4*B*. In WT fibers, R = 0.42 (P < 0.0001); in Homer $2^{-/-}$ FDB fibers, R = 0.30 (P < 0.0001). Spearman's rank correlation. FDB, flexor digitorum brevis; nAChR, nicotinic acetylcholine receptor; WT, wild type.

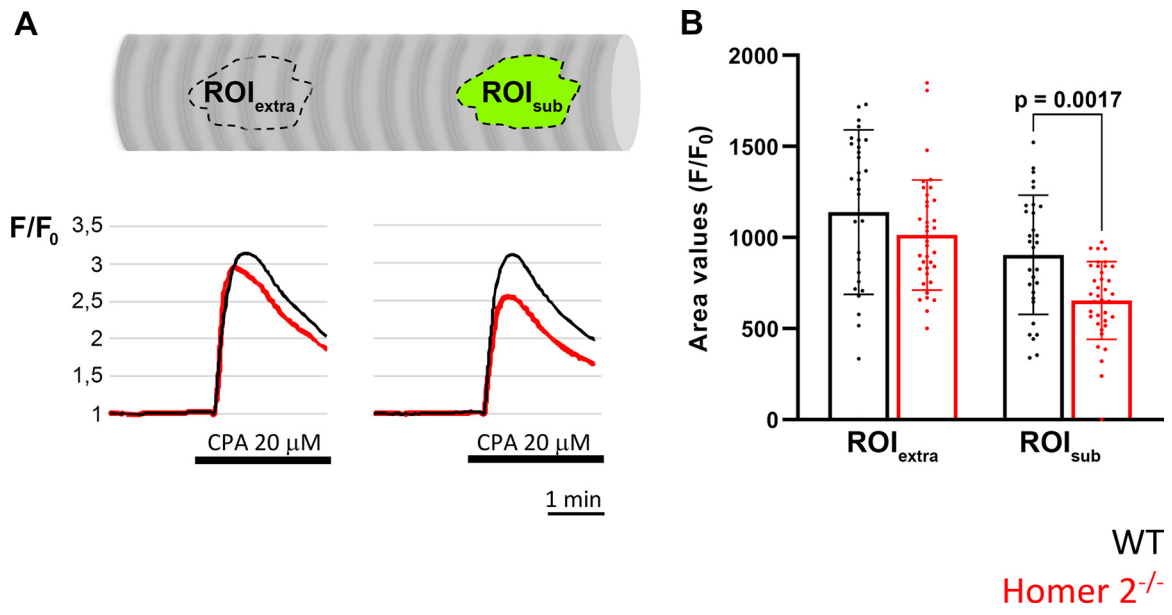

Figure 7. Subsynaptic Ca^{2+}-releasable pool in FDB fibers from WT and Homer 2$^{-/-}$ mice. *A*: representative $[Ca^{2+}]_i$ transients elicited by 20 µM CPA recorded in extrasynaptic and subsynaptic regions of interest (ROI_{extra} and ROI_{sub}) from a WT and Homer 2$^{-/-}$ FDB fibers. *B*: scatter plot of normalized area values of the CPA-induced $[Ca^{2+}]_i$ changes in paired ROI_{extra} and ROI_{sub} from WT and Homer 2$^{-/-}$ FDB fibers. Values are shown as means ± SD and correspond to: WT ROI_{extra} = 1,139.00 ± 451.00 vs. Homer 2$^{-/-}$ ROI_{extra} = 1,013.00 ± 302.90, WT ROI_{sub} = 904.50 ± 327.20 vs. Homer 2$^{-/-}$ ROI_{sub} = 654.60 ± 213.30. Data were from 35 WT FDB fibers (4 mice) and from 40 Homer 2$^{-/-}$ FDB fibers (4 mice). Statistical differences were determined by the Mann–Whitney *U* test. CPA, cyclopiazonic acid; FDB, flexor digitorum brevis; WT, wild type.

nAChRs. Analysis of the super-resolution fluorescent images revealed a clear prevalence of the CaMKIIβ-staining in the synaptic region in FDB fibers of WT mice. In contrast, synaptic CaMKIIβ-immunolabeling was almost indistinguishable from extrasynaptic regions in FDB fibers of Homer 2$^{-/-}$ mice (Fig. 8). The nAChRs/CaMKIIβ colocalization was evaluated by calculating the Manders's coefficient (i.e., the proportion of nAChRs stained voxels positive for CaMKIIβ). Manders' coefficients showed that the colocalization between two fluorescent signals was significantly lower in FDB fibers from Homer 2$^{-/-}$ mice compared with WT mice (Fig. 9*A*). This difference in colocalization was clearly visible in three-dimensional reconstructions of endplates from WT and Homer 2$^{-/-}$ mice (Fig. 9*B*).

Overall, these observations indicate that the absence of Homer 2 alters CaMKIIβ distribution, significantly reducing its colocalization with synaptic nAChRs. This change may impact synaptic function at the neuromuscular junction.

Electromyography and Motor Performance in Homer 2$^{-/-}$ Mice

Finally, experiments were conducted to study the effect of the Homer 2 ablation at the functional level.

Muscle electrical activity was recorded by EMG in FDB fibers from WT and Homer 2$^{-/-}$ mice. In both experimental groups, we measured CMAPs using repetitive nerve stimulation. At 10 and 30 Hz stimulation frequencies, a progressive reduction of CMAP amplitudes due to neuromuscular fatigue was observed. However, there are no statistical differences between WT and Homer 2$^{-/-}$ mice (Fig. 10*A*).

We also evaluated motor performance by the wire hanging and rotarod tests. The results of the wire hanging performance revealed that the latency to fall was characterized by a higher variability in Homer 2$^{-/-}$ compared with WT mice. However, the analysis did not reveal a statistical difference, indicating a comparable muscle endurance (Fig. 10*B*). Conversely, when placed on an accelerating rotarod, Homer 2$^{-/-}$ mice displayed a significantly shorter latency to fall as compared with WT$^{-/-}$ mice: this suggests a deficit in balance, coordination, and/or motor planning (Fig. 10*B*). Therefore, Homer 2 ablation appears to clearly emerge when the motor circuits that control overall movement are activated.

DISCUSSION

The scaffolding Homer 2 protein is emerging as one of the key players involved in NMJ plasticity, particularly after denervation and disuse. Our findings demonstrate that Homer 2 ablation and subsequent chronic adaptation led to a significant impairment in the endplate dynamics, characterized by a slower nAChR turnover and an altered organization of the subsynaptic IP_3-driven Ca^{2+} signaling machinery. These results highlight the crucial role of Homer 2 in maintaining NMJ integrity and function, suggesting potential therapeutic targets for neuromuscular disorders.

The first observation is a reduced nAChR channel activity, as judged by electrophysiological recordings. The exclusive presence of the adult ε-nAChR isoform in Homer 2$^{-/-}$ fibers (19), the absence of specific biomarkers (N-CAM and MHC-emb), and the similar circulating CAF levels in both WT and Homer 2$^{-/-}$ mice ruled out any contribution of "anatomical" and "functional" denervation.

Instead, the reduced nAChR activity is fully consistent with the second observation, that is, impaired endplate dynamics, as inferred from the slower insertion of new nAChRs in NMJs of Homer 2$^{-/-}$ mice. At *day 4*, α-BTX 488

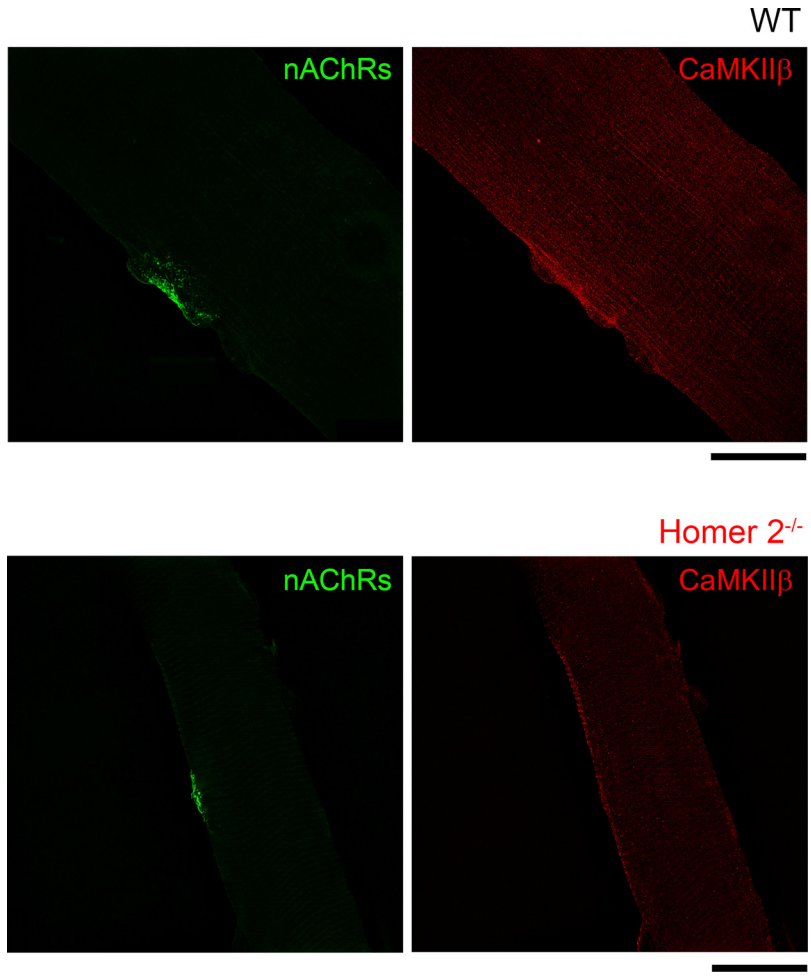

Figure 8. Distribution of CAMKIIβ in FDB fibers of WT and Homer 2$^{-/-}$ mice. Super-resolution fluorescence images revealed an accumulation of CaMKIIβ at the level of the endplate in WT fibers that was difficult to appreciate in Homer 2$^{-/-}$ counterparts. WT and Homer 2$^{-/-}$ images are shown as maximum intensity projections of the green and red voxels. The total number of projected plans was 52 for WT and 19 for Homer 2$^{-/-}$ images, respectively. Scale bar, 10 µm. FDB, flexor digitorum brevis; WT, wild type.

intensity corresponding to newly inserted nAChRs was lower in NMJs of Homer 2$^{-/-}$ than in WT ones, suggesting a deficit in the insertion of receptors. At *day 10*, the fluorescence intensity differences between the two experimental groups became undetectable: the deficit in the receptor turnover appears to reflect a delay rather than a permanent impairment. The significant upregulation of the AChRα1 gene, which was interpreted as a compensatory mechanism, excludes an impairment in the expression of the nAChRs and further validates the results of the turnover assay, which indicate a deficient nAChR incorporation into the endplate. The delayed nAChR incorporation perfectly aligns with the

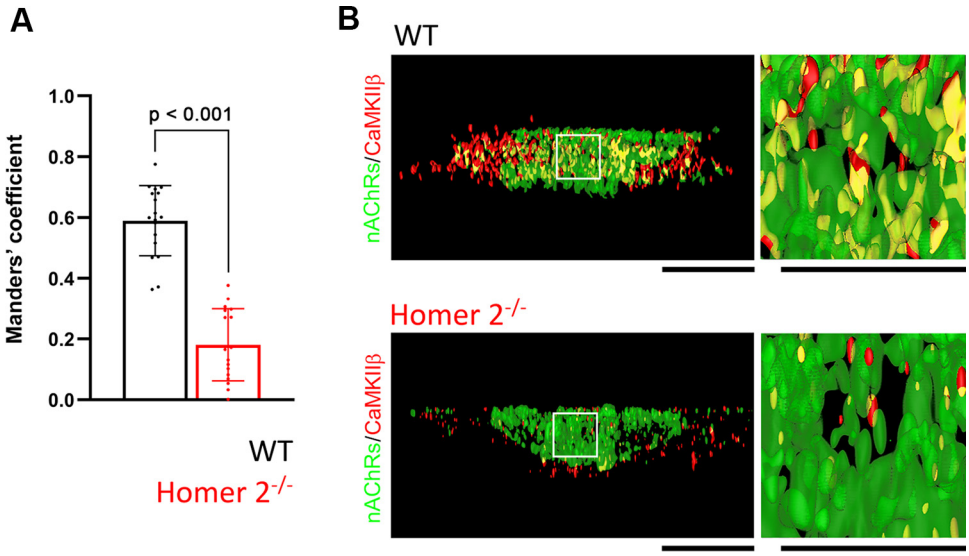

Figure 9. Colocalization of CAMKIIβ with nAChRs in FDB fibers of WT and Homer 2$^{-/-}$mice. *A*: scatter plot of the Manders' coefficients calculated for WT and Homer 2$^{-/-}$ FDB fibers. Colocalization was quantified as described in MATERIALS AND METHODS. Values are shown as means ± SD and correspond to: WT = 0.59 ± 0.11 (18 fibers, 3 mice); Homer 2$^{-/-}$ = 0.18 ± 0.12 (17 fibers, 3 mice). Statistical differences were determined by the Mann–Whitney *U* test. *B*: three-dimensional reconstruction of representative endplates and corresponding synaptic CaMKIIβ distribution in FDB fibers from WT and Homer 2$^{-/-}$ mice. Yellow indicates nAChRs/CaMKIIβ overlapping. Boxed areas (×2) are enlarged regions of the endplates, which allow focusing on the colocalization. Scale bar, 10 µm. CaMKIIβ, Ca^{2+}/calmodulin-dependent protein kinase IIβ; FDB, flexor digitorum brevis; nAChRs, nicotinic acetylcholine receptors; WT, wild type.

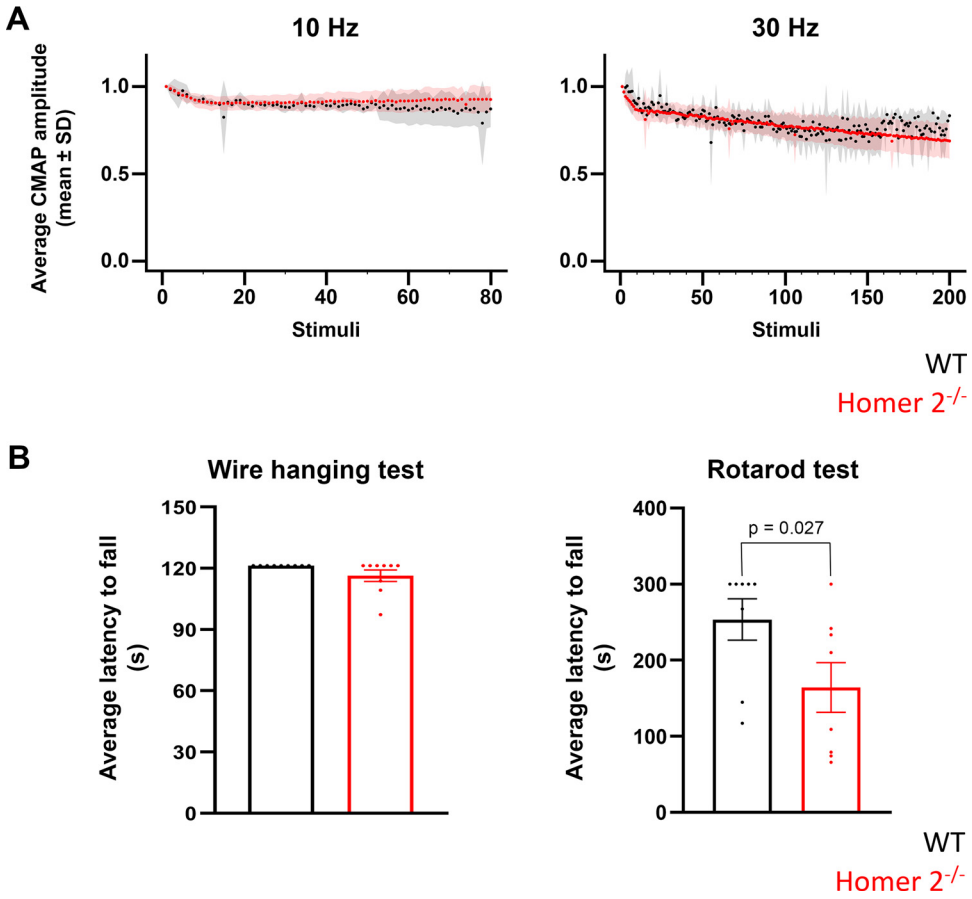

Figure 10. EMG and motor performance of WT and Homer 2$^{-/-}$ mice. *A*: amplitude of CMAPs recorded by EMG in the FDB muscle of WT and Homer 2$^{-/-}$ mice at 10 and 30 Hz nerve stimulation. The amplitude of the first CMAP of the repetitive responses was normalized to 1 (values are shown as means ± SD, see ribbons). Recordings showed a similar progressive reduction of CMAPs. Experiments were carried out on FDB muscles from six WT and seven Homer 2$^{-/-}$ mice for 10 Hz stimulation, and from three WT and five Homer 2$^{-/-}$ mice for 30 Hz stimulation. *B*: wire hanging test revealed a similar latency to fall for WT (120 ± 0.00, $n = 9$) and Homer 2$^{-/-}$ mice (115.22 ± 8.41, $n = 9$). Rotarod test showed a shorter latency to fall for Homer 2$^{-/-}$ mice (253.63 ± 76.98, $n = 8$) compared with WT mice (164.12 ± 92.14, $n = 8$). Values are shown as means ± SD, and statistical differences were determined by the Mann–Whitney *U* test. CMAP, compound muscle action potential; EMG, electromyography; FDB, flexor digitorum brevis; WT, wild type.

reduced endplate volume already described in Homer 2$^{-/-}$ mice (19).

In WT FDB muscle fibers, previous studies have reported that innervation controls the ratio between endplate volume and the corresponding subsynaptic volume stained for IP_3R1, the latter being ~40% of the corresponding endplate volume (7). Interestingly, both the endplate volume and the corresponding subsynaptic IP_3R1-stained volume were decreased by the same extent (~30%) in FDB fibers of Homer 2$^{-/-}$ mice. Despite this reduction, the ratio between the endplate size and the corresponding subsynaptic IP_3R1-immunolabeling, previously observed in WT counterparts, was maintained: the smaller the endplate, the smaller the subsynaptic IP_3R1-stained volume. This observation is consistent with the absence of denervation signs and the maintained innervation-controlled nAChRs/IP_3Rs cross talk (7) in Homer 2$^{-/-}$ mice, indicating that Homer 2 may be dispensable for certain aspects of NMJ integrity; on the contrary, it unveils a pivotal role of Homer 2 in determining size and dynamics of the endplate as well as controlling postsynaptic IP_3R1-associated local Ca^{2+} signals (5, 6).

Homers have been shown to participate in targeting and localization of Ca^{2+} signaling proteins to specific cellular microdomains, that is, the subsynaptic domain of synapses: Homer 2 might play a role at NMJs similar to that of Homer 1 isoforms in the postsynaptic density of excitatory central synapses. Indeed, in glutamatergic synapses, Homer 1 proteins play a crucial role in synaptic organization. The constitutive (Homer 1b/c) and inducible (Homer 1a) isoforms of Homer 1 physically bridge several molecules in the postsynaptic density, a protein-rich region just beneath the postsynaptic membrane. These molecules include metabotropic glutamate receptor types 1 and 5, as well as IP_3Rs (32). Through these interactions, Homer 1 proteins regulate glutamate receptor trafficking and synaptic remodeling (33). Furthermore, Homer 1, together with the scaffolding Shank1 protein, controls the recruitment of IP_3 receptors and endoplasmic reticulum cisternae within dendritic spines (34, 35). Similarly, Homer 2 appears to be a key controller of proper postsynaptic nAChR turnover and the correct organization of the subsynaptic IP_3-sensitive compartment.

Reduced subsynaptic IP_3R1-immunolabeling and reduced subsynaptic IP_3-releasable Ca^{2+} content point to a local impaired Ca^{2+} signaling and activation of downstream Ca^{2+} sensors as plausible reasons for the slower incorporation of nAChRs into the endplate in FDB fibers of Homer 2$^{-/-}$ mice. The proposed role for CaMKIIβ in regulating nAChR dynamics at the endplate and its tight clustering with nAChRs (31) prompted an investigation on FDB fibers of Homer 2$^{-/-}$mice: in fact, it was found that CaMKIIβ colocalizes much less with nAChRs in Homer 2 null mice than in WT ones. Bruneau et al. (3) have shown that insertion of both neo-synthesized and rapidly recycling AChRs contributes to the postsynaptic receptor density. Since the turnover assay used in this article cannot distinguish between the two pools, receptors indicated as "newly inserted" potentially include both groups. Notwithstanding, since CaMKIIβ has been demonstrated to have a crucial role in controlling the nAChR recycling (31),

the reduced endplate size in FDB fibers of Homer 2$^{-/-}$ mice may be primarily the result of a slower delivery of recycling nAChRs into the endplate. Consequently, Homer 2 could contribute to nAChR dynamics by also regulating the correct localization of CaMKIIβ at the endplate.

It must be emphasized that, apart from CaMKIIβ, several other important players control nAChR turnover: Rapsyn serves as a master regulator of nAChR clustering and NMJ formation (reviewed in Ref. 36); PKA promotes the stability of endplate nAChRs and prevents the removal of recycled nAChRs from the postsynaptic membrane (37); PKC promotes removal of nAChRs from postsynaptic sites and regulates the nAChR recycled pool by reducing the half-life of recycled receptors in the postsynaptic membrane (37); Myosin Va controls nAChR recycling, possibly by restraining endocytic/recycling vesicles near the postsynaptic membrane in an activity-dependent cAMP microdomain (reviewed in Ref. 38). Each of these players merits investigation through dedicated experiments to fully elucidate the mechanism(s) through which Homer 2 contributes to nAChR turnover.

NMJ adaptation is by no means a single pathophysiological process, given its multiple etiologies and possibly distinct pathogenic mechanisms. For example, denervation typically leads to motor endplate adaptation, resulting from accelerated turnover of nAChRs (12, 39). In Homer 2$^{-/-}$ mice, instead, the dynamics of nAChRs are slowed, that is, pathogenesis is clearly different and leads to a distinct picture of NMJ adaptation. In any case, this article shows for the first time that Homer 2 holds a major role in the regulation of the recycling/insertion receptor dynamics.

Denervation consistently causes muscle atrophy, whereas in Homer 2$^{-/-}$ mice, atrophy was observed in predominantly slow-twitch muscles, for example, soleus, but not in predominantly fast-twitch muscles, extensor digitorum longus and FDB (19). The apparent discrepancy could be accounted for considering that: *1*) a safety factor enables motoneurons to trigger superthreshold endplate potentials and muscle-spiking activity with only 10%–20% of receptors being activated (40) and *2*) the safety factor is significantly larger in fast-twitch muscles (41). Consequently, although the more severe destabilization culminating in the endplate fragmentation observed after denervation could not be compensated by the safety factor in all muscles, the less severe reduction in volume due to the reduced nAChRs recycling/insertion could be fully compensated by the larger safety factor only in predominantly fast-twitch muscles.

Similarly, the peculiar superthreshold postsynaptic potential could explain why the functional effect of reduced nAChR recycling/insertion is not detectable when neuromuscular fatigue and muscle endurance were evaluated by EMG and wire hanging tests, respectively. Therefore, the lack of measurable atrophy (19) and impaired neuromuscular transmission (present data) should not be taken as evidence that Homer 2 plays a superfluous role in nAChR turnover in skeletal muscle fibers. Intriguingly, the effect of the Homer 2 ablation stands out during the accelerating rotarod assessment, i.e., when activation of central motor circuits is brought into the picture. This serendipitous finding suggests a putative, yet unexplored role for Homer 2 scaffolding in the central nervous system.

Conclusive Remarks: A New Type of NMJ Instability in Homer 2$^{-/-}$ Mice

One of the fundamental properties of skeletal muscle NMJ is stability, that is, its ability to maintain functional and structural integrity overtime, ensuring effective transmission of nerve impulses from the motor neuron to the muscle fibers. Stability depends on several factors: *1*) structural integrity of the presynaptic (nerve terminal), synaptic (synaptic cleft), and postsynaptic (motor endplate) components; *2*) molecular balance among key proteins such as acetylcholinesterase or nAChRs; *3*) synaptic plasticity, that is, reversible adaptation to both physiological and pathological stimuli; *4*) active maintenance through continuous remodeling and repair mediated

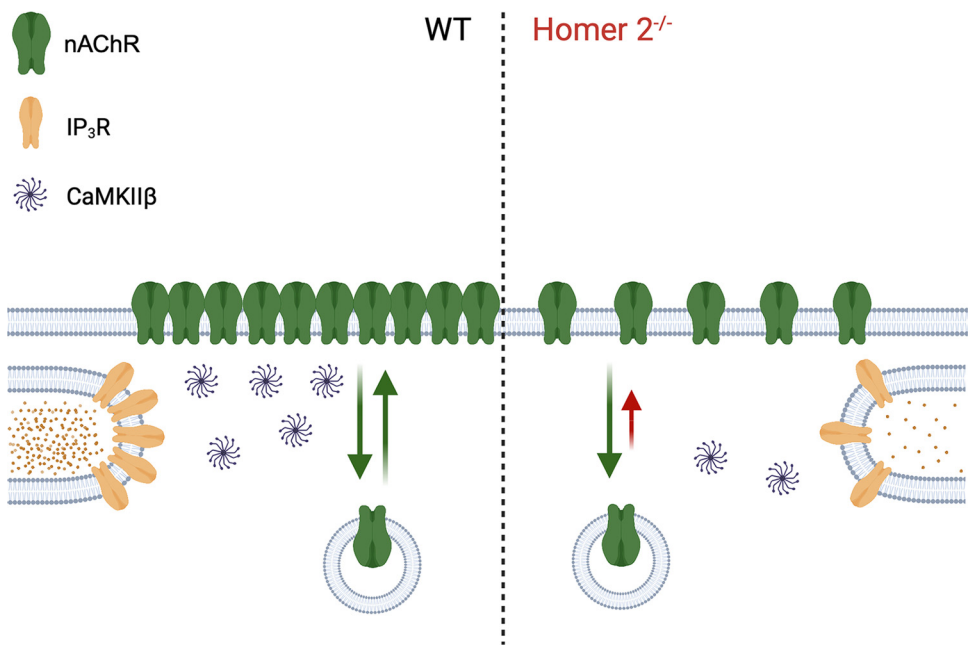

Figure 11. Comparison of the subsynaptic molecular machinery of WT and Homer 2$^{-/-}$ mice. The figure illustrates the adaptive effects caused by the absence of Homer 2 on the subsynaptic molecular machinery and the resulting impaired incorporation of the nAChRs into the membrane: this may be one of the putative mechanisms for the reduced number of nAChRs at the NMJ of Homer 2$^{-/-}$ mice (figure created with a licensed version of BioRender.com). nAChRs, nicotinic acetylcholine receptors; NMJ, neuromuscular junction; WT, wild type.

by either nerve activity, trophic signals, or growth factors; and *5*) stress resistance, that is the ability to preserve function even under conditions of either mechanical or metabolic stress (12).

The steady-state of nAChRs, one of the features of stability, is maintained by the dynamic equilibrium between five main processes: synthesis, lateral diffusion, internalization, degradation, and recycling. Dynamics of nAChRs specifically refers to processes that maintain the density of nAChRs in the NMJ (2, 31, 37).

According to Sirago et al. (42), instability of NMJ concerns any process underlying detectable changes in NMJ homeostasis, at the structural and/or functional level: full-fledged instability of NMJ clearly occurs after denervation or in skeletal muscle disuse and is accompanied by impaired nerve transmission. In this article, a second and new type of NMJ instability is proposed based on the presence or absence of signs of denervation: classical models of denervation and oncogenic cachexia (see Ref. 43) belong to the first group, whereas the Homer 2$^{-/-}$ mouse model belongs to the second group.

Based on previous and current experimental findings, ablation of Homer 2 leads to chronic NMJ adaptation characterized by decreased number of nAChRs in the presence of normal innervation. Altered dynamics of nAChRs appear to be due to decreased insertion of nAChRs, namely decreased recycling.

By and large, our data confirm the role of Homer 2 in NMJ adaptation (16, 19) and shed new light on its role in controlling the dynamics of NMJ at the postsynaptic level. The scaffold protein Homer 2 emerges as an important player in the regulation of nAChRs incorporation into the endplate, by controlling the subsynaptic IP_3R1 content, the IP_3-releasable Ca^{2+} pool, and the colocalization of CaMKIIβ with nAChRs (Fig. 11). Although this is the first report demonstrating a role for Homer 2 in controlling endplate nAChRs dynamics, we acknowledge that our findings are limited by an incomplete understanding of Homer 2 interacting partners and downstream effectors. Further studies are necessary to fully characterize the role of Homer 2 in NMJ physiology, plasticity, and pathology. In conclusion, these findings not only advance the understanding of NMJ dynamics but also open new avenues for investigating neuromuscular disorders and developing potential therapeutic strategies targeting Homer 2-mediated pathways.

DATA AVAILABILITY

Data will be made available upon reasonable request.

ACKNOWLEDGMENTS

The authors thank Dr. Alessandra Bosutti (University of Trieste), Riccardo Filadi, and Paola Pizzo (University of Padova) for performing preliminary experiments.

GRANTS

This research was funded by the University of Trieste, Italy (Bando straordinario per il finanziamento dell'acquisto di attrezzature specifiche—Anno 2022—Prot n. 96508, dated July 11, 2022) and supported by Grants ASI 2018-13-U.0-NEMUCO and 2023-13-U.0-NEMUSY (to P.V. and P.L.).

DISCLOSURES

No conflicts of interest, financial or otherwise, are declared by the authors.

AUTHOR CONTRIBUTIONS

P.L. and P.V. conceived and designed research; P.L., S.A., S.F., B.R., A.B., M.S., R.S., A.M., and A.N. performed experiments; P.L., S.A., S.F., B.R., A.B., M.S., R.S., A.M., S.Z., and A.N. analyzed data; P.L., S.A., S.F., B.R., A.B., M.S., R.S., A.M., S.Z., and A.N. interpreted results of experiments; P.L., S.A., S.F., B.R., A.B., A.M., and S.Z. prepared figures; P.L., S.A., S.F., A.B., S.Z., and P.V. drafted manuscript; P.L. and P.V. edited and revised manuscript; P.L., S.A., S.F., B.R., A.B., M.S., R.S., A.M., S.Z., and P.V. approved final version of manuscript.

REFERENCES

1. **Bruneau EG**, **Akaaboune M.** Running to stand still: ionotropic receptor dynamics at central and peripheral synapses. *Mol Neurobiol* 34: 137–151, 2006. doi:10.1385/MN:34:2:137.
2. **Bruneau EG**, **Akaaboune M.** The dynamics of recycled acetylcholine receptors at the neuromuscular junction in vivo. *Development* 133: 4485–4493, 2006. doi:10.1242/dev.02619.
3. **Bruneau E**, **Sutter D**, **Hume RI**, **Akaaboune M.** Identification of nicotinic acetylcholine receptor recycling and its role in maintaining receptor density at the neuromuscular junction in vivo. *J Neurosci* 25: 9949–9959, 2005. doi:10.1523/JNEUROSCI.3169-05.2005.
4. **Strack S**, **Petersen Y**, **Wagner A**, **Röder IV**, **Albrizio M**, **Reischl M**, **Wacker IU**, **Wilhelm C**, **Rudolf R.** A novel labeling approach identifies three stability levels of acetylcholine receptors in the mouse neuromuscular junction in vivo. *PLoS One* 6: e20524, 2011. doi:10.1371/journal.pone.0020524.
5. **Zayas R**, **Groshong JS**, **Gomez CM.** Inositol-1, 4, 5-triphosphate receptors mediate activity induced synaptic Ca^{2+} signals in muscle fibers and Ca^{2+} overload in slow-channel syndrome. *Cell Calcium* 41: 343–352, 2007. doi:10.1016/j.ceca.2006.07.007.
6. **Zhu H**, **Bhattacharyya BJ**, **Lin H**, **Gomez CM.** Skeletal muscle IP_3R1 receptors amplify physiological and pathological synaptic calcium signals. *J Neurosci* 31: 15269–15283, 2011. doi:10.1523/JNEUROSCI.3766-11.2011.
7. **Volpe P**, **Bosutti A**, **Nori A**, **Filadi R**, **Gherardi G**, **Trautmann G**, **Furlan S**, **Massaria G**, **Sciancalepore M**, **Megighian A**, **Caccin P**, **Bernareggi A**, **Salanova M**, **Sacchetto R**, **Sandonà D**, **Pizzo P**, **Lorenzon P.** Nerve-dependent distribution of subsynaptic type 1 inositol 1,4,5-trisphosphate receptor at the neuromuscular junction. *J Gen Physiol* 154: e202213128, 2022. doi:10.1085/jgp.202213128.
8. **De Koninck P**, **Schulman H.** Sensitivity of CaM kinase II to the frequency of Ca^{2+} oscillations. *Science* 279: 227–230, 1998. doi:10.1126/science.279.5348.227.
9. **Sacchetto R**, **Bovo E**, **Damiani E.** The Ca^{2+}-calmodulin dependent protein kinase II system of skeletal muscle sarcoplasmic reticulum. *Basic Appl Myol* 15: 5–17, 2005.
10. **Aydin J**, **Korhonen T**, **Tavi P**, **Allen DG**, **Westerblad H**, **Bruton JD.** Activation of Ca^{2+}-dependent protein kinase II during repeated contractions in single muscle fibres from mouse is dependent on the frequency of sarcoplasmic reticulum Ca^{2+} release. *Acta Physiol (Oxf)* 191: 131–137, 2007 [Erratum in *Acta Physiol (Oxf)* 193: 199, 2008]. doi:10.1111/j.1748-1716.2007.01725.x.
11. **Kramerova I**, **Torres JA**, **Eskin A**, **Nelson SF**, **Spencer MJ.** Calpain 3 and CaMKIIβ signaling are required to induce HSP70 necessary for adaptive muscle growth after atrophy. *Hum Mol Genet* 27: 1642–1653, 2018. doi:10.1093/hmg/ddy071.
12. **Martinez-Pena Y Valenzuela I**, **Akaaboune M.** The metabolic stability of the nicotinic acetylcholine receptor at the neuromuscular junction. *Cells* 10: 358, 2021. doi:10.3390/cells10020358.

13. **Falcetta D**, **Quirim S**, **Cocchiararo I**, **Chabry F**, **Théodore M**, **Stiefvater A**, **Lin S**, **Tintignac L**, **Ivanek R**, **Kinter J**, **Rüegg MA**, **Sinnreich M**, **Castets P.** CaMKIIβ deregulation contributes to neuromuscular junction destabilization in myotonic dystrophy type I. *Skelet Muscle* 14: 11, 2024. doi:10.1186/s13395-024-00345-3.
14. **Salanova M**, **Bortoloso E**, **Schiffl G**, **Gutsmann M**, **Belavy DL**, **Felsenberg D**, **Furlan S**, **Volpe P**, **Blottner D.** Expression and regulation of Homer in human skeletal muscle during neuromuscular junction adaptation to disuse and exercise. *FASEB J* 25: 4312–4325, 2011. doi:10.1096/fj.11-186049.
15. **Bortoloso E**, **Megighian A**, **Furlan S**, **Gorza L**, **Volpe P.** Homer 2 antagonizes protein degradation in slow-twitch skeletal muscles. *Am J Physiol Cell Physiol* 304: C68–C77, 2013. doi:10.1152/ajpcell.00108.2012.
16. **Salanova M**, **Volpe P**, **Blottner D.** Homer protein family regulation in skeletal muscle and neuromuscular adaptation. *IUBMB Life* 65: 769–776, 2013. doi:10.1002/iub.1198.
17. **Salanova M**, **Priori G**, **Barone V**, **Intravaia E**, **Flucher B**, **Ciruela F**, **McIlhinney RA**, **Parys JB**, **Mikoshiba K**, **Sorrentino V.** Homer proteins and $InsP_3$ receptors co-localise in the longitudinal sarcoplasmic reticulum of skeletal muscle fibres. *Cell Calcium* 32: 193–200, 2002. doi:10.1016/s0143416002001549.
18. **Shin DM**, **Dehoff M**, **Luo X**, **Hyeok Kang S**, **Tu J**, **Nayak SK**, **Ross EM**, **Worley PF**, **Muallem S.** Homer 2 tunes G protein–coupled receptors stimulus intensity by regulating RGS proteins and PLCβ GAP activities. *J Cell Biol* 162: 293–303, 2003. doi:10.1083/jcb.200210109.
19. **Lorenzon P**, **Furlan S**, **Ravara B**, **Bosutti A**, **Massaria G**, **Bernareggi A**, **Sciancalepore M**, **Trautmann G**, **Block K**, **Blottner D**, **Worley PF**, **Zampieri S**, **Salanova M**, **Volpe P.** Preliminary observations on skeletal muscle adaptation and plasticity in homer $2^{-/-}$ mice. *Metabolites* 11: 642, 2021. doi:10.3390/metabo11090642.
20. **Schubert M**, **Pelz A**, **Trautmann G**, **Block K**, **Furlan S**, **Gutsmann M**, **Kohler S**, **Volpe P**, **Blottner D**, **Meisel A**, **Salanova M.** Opposite regulation of homer signal at the NMJ postsynaptic micro domain between slow- and fast-twitch muscles in an experimentally induced autoimmune myasthenia gravis (EAMG) mouse model. *Int J Mol Sci* 23: 15052, 2022. doi:10.3390/ijms232315052.
21. **Grohovaz F**, **Lorenzon P**, **Ruzzier F**, **Zorec R.** Properties of acetylcholine receptors in adult rat skeletal muscle fibers in culture. *J Membr Biol* 136: 31–42, 1993. doi:10.1007/BF00241487.
22. **Gambara G**, **Salanova M**, **Ciciliot S**, **Furlan S**, **Gutsmann M**, **Schiffl G**, **Ungethuem U**, **Volpe P**, **Gunga HC**, **Blottner D.** Microgravity-induced transcriptome adaptation in mouse paraspinal longissimus dorsi muscle highlights insulin resistance-linked genes. *Front Physiol* 8: 279, 2017. doi:10.3389/fphys.2017.00279.
23. **Röder IV**, **Petersen Y**, **Choi KR**, **Witzemann V**, **Hammer JA III**, **Rudolf R.** Role of Myosin Va in the plasticity of the vertebrate neuromuscular junction in vivo. *PLoS One* 3: e3871, 2008. doi:10.1371/journal.pone.0003871.
24. **Zelada D**, **Barrantes FJ**, **Henríquez JP.** Lithium causes differential effects on postsynaptic stability in normal and denervated neuromuscular synapses. *Sci Rep* 11: 17285, 2021. doi:10.1038/s41598-021-96708-7.
25. **Schindelin J**, **Arganda-Carreras I**, **Frise E**, **Kaynig V**, **Longair M**, **Pietzsch T**, **Preibisch S**, **Rueden C**, **Saalfeld S**, **Schmid B**, **Tinevez JY**, **White DJ**, **Hartenstein V**, **Eliceiri K**, **Tomancak P**, **Cardona A.** Fiji: an open-source platform for biological-image analysis. *Nat Methods* 9: 676–682, 2012. doi:10.1038/nmeth.2019.
26. **Volpe P**, **Biral D**, **Pizzo P**, **Salviati G**, **Margreth A.** Ontogenesis of chick iris intrinsic muscles: evidence for a smooth-to-striated muscle transition. *Dev Biol* 159: 441–449, 1993. doi:10.1006/dbio.1993.1254.
27. **Covault J**, **Sanes JR.** Neural cell adhesion molecule (N-CAM) accumulates in denervated and paralyzed skeletal muscles. *Proc Natl Acad Sci USA* 82: 4544–4548, 1985. doi:10.1073/pnas.82.13.4544.
28. **Bolliger MF**, **Zurlinden A**, **Lüscher D**, **Bütikofer L**, **Shakhova O**, **Francolini M**, **Kozlov SV**, **Cinelli P**, **Stephan A**, **Kistler AD**, **Rülicke T**, **Pelczar P**, **Ledermann B**, **Fumagalli G**, **Gloor SM**, **Kunz B**, **Sonderegger P.** Specific proteolytic cleavage of agrin regulates maturation of the neuromuscular junction. *J Cell Sci* 123: 3944–3955, 2010. doi:10.1242/jcs.072090.
29. **Hettwer S**, **Dahinden P**, **Kucsera S**, **Farina C**, **Ahmed S**, **Fariello R**, **Drey M**, **Sieber CC**, **Vrijbloed JW.** Elevated levels of a C-terminal agrin fragment identifies a new subset of sarcopenia patients. *Exp Gerontol* 48: 69–75, 2013. doi:10.1016/j.exger.2012.03.002.
30. **Monti E**, **Reggiani C**, **Franchi MV**, **Toniolo L**, **Sandri M**, **Armani A**, **Zampieri S**, **Giacomello E**, **Sarto F**, **Sirago G**, **Murgia M**, **Nogara L**, **Marcucci L**, **Ciciliot S**, **Simunic B**, **Pišot R**, **Narici MV.** Neuromuscular junction instability and altered intracellular calcium handling as early determinants of force loss during unloading in humans. *J Physiol* 599: 3037–3061, 2021. doi:10.1113/JP281365.
31. **Martinez-Pena y Valenzuela I**, **Mouslim C**, **Akaaboune M.** Calcium/calmodulin kinase II-dependent acetylcholine receptor cycling at the mammalian neuromuscular junction in vivo. *J Neurosci* 30: 12455–12465, 2010. doi:10.1523/JNEUROSCI.3309-10.2010.
32. **de Bartolomeis A**, **Barone A**, **Buonaguro EF**, **Tomasetti C**, **Vellucci L**, **Iasevoli F.** The Homer1 family of proteins at the crossroad of dopamine-glutamate signaling: an emerging molecular "Lego" in the pathophysiology of psychiatric disorders. A systematic review and translational insight. *Neurosci Biobehav Rev* 136: 104596, 2022. doi:10.1016/j.neubiorev.2022.104596.
33. **Clifton NE**, **Trent S**, **Thomas KL**, **Hall J.** Regulation and function of activity-dependent homer in synaptic plasticity. *Mol Neuropsychiatry* 5: 147–161, 2019. doi:10.1159/000500267.
34. **Sala C**, **Piëch V**, **Wilson NR**, **Passafaro M**, **Liu G**, **Sheng M.** Regulation of dendritic spine morphology and synaptic function by Shank and Homer. *Neuron* 31: 115–130, 2001. doi:10.1016/s0896-6273(01)00339-7.
35. **Sala C**, **Roussignol G**, **Meldolesi J**, **Fagni L.** Key role of the postsynaptic density scaffold proteins Shank and Homer in the functional architecture of Ca^{2+} homeostasis at dendritic spines in hippocampal neurons. *J Neurosci* 25: 4587–4592, 2005. doi:10.1523/JNEUROSCI.4822-04.2005.
36. **Xing G**, **Xiong WC**, **Mei L.** Rapsyn as a signaling and scaffolding molecule in neuromuscular junction formation and maintenance. *Neurosci Lett* 731: 135013, 2020. doi:10.1016/j.neulet.2020.135013.
37. **Martinez-Pena y Valenzuela I**, **Pires-Oliveira M**, **Akaaboune M.** PKC and PKA regulate AChR dynamics at the neuromuscular junction of living mice. *PLoS One* 8: e81311, 2013. doi:10.1371/journal.pone.0081311.
38. **Rudolf R.** Myosin Va: capturing cAMP for synaptic plasticity. *Front Physiol* 14: 1342994, 2023. doi:10.3389/fphys.2023.1342994.
39. **Fumagalli G**, **Balbi S**, **Cangiano A**, **Lømo T.** Regulation of turnover and number of acetylcholine receptors at neuromuscular junctions. *Neuron* 4: 563–569, 1990. doi:10.1016/0896-6273(90)90114-u.
40. **Lingle CJ**, **Steinbach JH.** Neuromuscular blocking agents. *Int Anesthesiol Clin* 26: 288–301, 1988. doi:10.1097/00004311-198802640-00007.
41. **Wood SJ**, **Slater CR.** The contribution of postsynaptic folds to the safety factor for neuromuscular transmission in rat fast- and slow-twitch muscles. *J Physiol* 500: 165–176, 1997. doi:10.1113/jphysiol.1997.sp022007.
42. **Sirago G**, **Pellegrino MA**, **Bottinelli R**, **Franchi MV**, **Narici MV.** Loss of neuromuscular junction integrity and muscle atrophy in skeletal muscle disuse. *Ageing Res Rev* 83: 101810, 2023. doi:10.1016/j.arr.2022.101810.
43. **Sartori R**, **Hagg A**, **Zampieri S**, **Armani A**, **Winbanks CE**, **Viana LR**, **Haidar M**, **Watt KI**, **Qian H**, **Pezzini C**, **Zanganeh P**, **Turner BJ**, **Larsson A**, **Zanchettin G**, **Pierobon ES**, **Moletta L**, **Valmasoni M**, **Ponzoni A**, **Attar S**, **Da Dalt G**, **Sperti C**, **Kustermann M**, **Thomson RE**, **Larsson L**, **Loveland KL**, **Costelli P**, **Megighian A**, **Merigliano S**, **Penna F**, **Gregorevic P**, **Sandri M.** Perturbed BMP signaling and denervation promote muscle wasting in cancer cachexia. *Sci Transl Med* 13: eaay9592, 2021. doi:10.1126/scitranslmed.aay9592.